

Seasonally variant low cloud adjustment over cool oceans

Youichi Kamae^{1*}, Robin Chadwick², Duncan Ackerley³, Mark Ringer², and Tomoo Ogura⁴

¹Faculty of Life and Environmental Sciences, University of Tsukuba, Tsukuba, Ibaraki, Japan

²Met Office Hadley Centre, Exeter, Devon, UK

³Met Office, Exeter, Devon, UK

⁴National Institute for Environmental Studies, Tsukuba, Ibaraki, Japan

Submitted to *Climate Dynamics*

*Corresponding author: Youichi Kamae, Faculty of Life and Environmental Sciences, University of Tsukuba, 1-1-1 Tennoudai, Tsukuba, Ibaraki 305-8572, Japan (kamae.yoichi.fw@u.tsukuba.ac.jp), Tel.: +81-29-853-4755
Fax: +81-29-853-6709

18 **Abstract**

19 The Earth's solar reflectance is reduced through rapid climate adjustments to increasing CO₂, via a decrease
20 in total cloud cover over ocean. Perturbations to marine boundary-layer clouds are essentially important for the
21 global radiative balance at the top of the atmosphere. However, the physical robustness of low cloud adjustments
22 to increasing CO₂ has not been assessed systematically. Here we show that low cloud adjustment is distinct from
23 that in total cloud and is seasonally variant. Among multiple climate models, marine boundary-layer clouds over
24 the subtropics and extratropics (especially over the Northern Hemisphere) are consistently increased in the rapid
25 adjustment, while middle and high clouds are greatly reduced. The increase in low cloud cover is only found during
26 summer, associated with a summertime enhancement of lower tropospheric stability. We further examine
27 mechanisms behind the rapid adjustments of low cloud and inversion strength of the boundary layer, using land
28 surface temperature prescribing experiments in an atmospheric general circulation model (AGCM). Summertime
29 increases in low cloud and enhanced inversion strength over the ocean simulated in this AGCM are attributed to
30 (1) CO₂-induced land warming; and (2) reduced radiative cooling in the lower troposphere due to increased CO₂.
31 The seasonality in the cloud adjustment implies an importance of seasonal variations in background cloud and
32 atmospheric circulation related to the Hadley and monsoon circulations for radiative forcing, feedback and climate
33 sensitivity.

34 **Keywords:** Cloud adjustment, instantaneous radiative forcing, inversion strength, low cloud

35

36 **1. Introduction**

37 Cloud responses to external forcing (e.g. greenhouse gases and aerosols) imposed on the Earth's climate
38 system are very important for perturbing the radiative balance at the top of the atmosphere (TOA) and surface air
39 temperature (SAT). Clouds are the major source of uncertainty in estimating climate sensitivity, determined as
40 global-mean SAT increase in response to doubling of atmospheric CO₂ concentration (e.g. Cess et al. 1989;
41 Boucher et al. 2014; Bretherton 2015; Kamae et al. 2016a; Ceppi et al. 2017). By using numerical model
42 simulations, uncertainty in cloud response to CO₂ increases can be divided into two processes: fast cloud
43 adjustment to increasing CO₂; and slow cloud response mediated by global-mean SAT increase (Gregory and Webb
44 2008; Andrews et al. 2012; Kamae et al. 2015; Sherwood et al. 2015). There are large uncertainties across different
45 climate models for both processes (e.g. Vial et al. 2013; Webb et al. 2013; Zelinka et al. 2013). Previous studies
46 found that cloud adjustment and cloud feedback are anticorrelated among climate models, which is important for
47 the resultant uncertainty spread in climate sensitivity (Shiogama et al. 2012; Webb et al. 2013; Ringer et al. 2014).
48 Chung and Soden (2018) demonstrated that marine boundary-layer cloud is the key for the adjustment-feedback
49 compensation among multiple models that participated in the Coupled Model Intercomparison Project phase 5
50 (CMIP5; Taylor et al. 2012). However, physical mechanisms responsible for the compensation of cloud adjustment
51 and feedback are still unclear and further work is required to reduce the uncertainty.

52 Previous studies demonstrated that the key processes responsible for tropospheric cloud adjustments are:
53 the land-sea warming contrast related to the land response to increased CO₂ (Dong et al. 2009; Wyant et al. 2012;
54 Kamae and Watanabe 2013; Chadwick et al. 2014); tropospheric warming and resultant drying (Kamae and

55 Watanabe 2012; Kamae et al. 2015); and enhanced stability in lower troposphere due to tropospheric warming
56 (Webb et al. 2013; Ogura et al. 2014; Qu et al. 2015a). CO₂-induced land warming found in atmospheric general
57 circulation model (AGCM) simulations with prescribed sea surface conditions (temperature and sea ice) changes
58 the large-scale atmospheric circulation and induces tropospheric warming (Chadwick et al. 2014; He and Soden
59 2015, 2016; Shaw and Voigt 2015, 2016), which are important for cloud adjustments over land and ocean (Colman
60 and McAvaney 2011; Kamae and Watanabe 2012, 2013; Kamae et al. 2015). The land surface and atmosphere
61 above are also greatly influenced by the plant physiological response to imposed CO₂ forcing (reduced
62 evapotranspiration due to stomatal closure; e.g. Boucher et al. 2009; Doutriaux-Boucher et al. 2009; Abe et al.
63 2015), leading to reduced cloud cover over land (Andrews et al. 2012).

64 In addition to the land-mediated cloud responses, perturbations to the atmospheric radiative heating profile
65 due to increased CO₂ is also critically important for the cloud adjustment (see Fig. S1). Longwave radiative heating
66 (i.e. reduced radiative cooling of the troposphere; Sugi and Yoshimura 2004; Collins et al. 2006; Colman and
67 McAvaney 2011; Kamae and Watanabe 2013; Ogura et al. 2014; Merlis 2015) due to instantaneous radiative
68 forcing of CO₂ (Hansen et al. 2002) results in a shoaling of the planetary boundary layer (e.g. Watanabe et al. 2012;
69 Wyant et al. 2012; Bretherton et al. 2013; Kamae and Watanabe 2013; Zelinka et al. 2013) and reduction of total
70 cloud amount over the ocean, then increases effective radiative forcing of CO₂ via the tropospheric adjustment
71 (Kamae and Watanabe 2012; Bretherton et al. 2013; Zelinka et al. 2013; Kamae et al. 2015). However, modeled
72 low-cloud adjustment still shows a large spread among different modeling studies (Wyant et al. 2012; Bretherton

73 et al. 2014; Kamae et al. 2015; Blossey et al. 2016; Xu et al. 2018), suggesting uncertainty in the relative
74 importance of the physical processes discussed above.

75 One of the key limitations in our understanding of the cloud adjustment to imposed CO₂ forcing is due to
76 the difficulty in decomposing the adjustment into individual processes including atmospheric radiation, land
77 warming, and the plant physiological response. Shine et al. (2003) conducted a set of prescribed land temperature
78 experiments in an intermediate complexity GCM to estimate radiative forcing and climate sensitivity. In contrast
79 to fixed sea surface temperature (SST) simulations in AGCMs, such prescribed land temperature experiments are
80 useful to evaluate the effective radiative forcing independently from land surface warming. However, this method
81 has not been widely applied to the CMIP ensembles due to the technical difficulty in prescribing land surface
82 temperatures. Recently, Ackerley and Dommenges (2016) proposed a new method for decomposing the effects of
83 instantaneous radiative forcing, increases in SST, increases in land surface temperature, and the plant physiological
84 response from conventional AGCM simulations. Under this framework, Ackerley et al. (2018) conducted a suite
85 of AGCM simulations and made their output available for facilitating wider studies including those focusing on
86 atmospheric circulations and rainfall patterns (Chadwick et al. 2018). In our study, we aim to examine the physical
87 processes that control robust and uncertain parts of the cloud adjustment to increasing CO₂ by using the prescribed
88 land surface temperature simulations described in Ackerley et al. (2018). Results from these simulations clearly
89 show seasonal difference in the cloud and tropospheric temperature responses to seasonally-uniform CO₂ increases,
90 which is very important for the seasonal migration of the Intertropical Convergence Zone (ITCZ) and monsoons
91 (Kamae et al. 2014, 2016b; Shaw and Voigt 2015; Chen and Bordoni 2016; Chadwick et al. 2018). Seasonal

92 variations found here improve process-based understanding of cloud adjustments. Section 2 describes the data and
93 methods including multiple model simulations and prescribed land surface temperature experiments in an AGCM.
94 Section 3 compares cloud adjustments among different models, vertical levels and seasons. Section 4 provides
95 results of a decomposition of low cloud adjustment using a set of AGCM simulations. In Section 5, we discuss
96 possible reasons for the seasonal variation in cloud adjustment to a seasonally-uniform increase in CO₂
97 concentration. Section 6 is a summary with discussion.

98

99 **2. Data and methods**

100 **2.1. CMIP5 model simulations**

101 To examine the robustness of cloud adjustments, we use the results of multiple model simulations conducted
102 under CMIP5 (Taylor et al. 2012). We use results from sstClim and sstClim4xCO₂ runs conducted in 15 AGCMs
103 (Table S1). The rapid adjustments of lower tropospheric stability and low cloud fraction over ocean found in these
104 AGCM-based simulations are consistent with those found in atmosphere-ocean coupled model simulations forced
105 by abruptly increased CO₂ concentration (e.g. Kamae and Watanabe 2013; Kamae et al. 2015; Qu et al. 2015a). In
106 sstClim, AGCMs were driven by climatological SSTs and sea-ice concentrations derived from pre-industrial
107 control simulations in each model. Boundary conditions for sstClim4xCO₂ are identical to sstClim except for
108 atmospheric CO₂ concentration (280 and 1120 ppmv in sstClim and sstClim4xCO₂, respectively). In this study,
109 we examine differences (Δ hereafter) of climatology (averaged over 30 years) between the two simulations.
110 Seasonal variations in cloud adjustment at different vertical levels are investigated by monthly-mean cloud fraction

111 at each model layer (note that the number of model layers are different across models; see Table S1). The CMIP5
112 data portal did not archive diagnostics of low, middle and high cloud fraction. In this study, we approximate low,
113 middle and high cloud fraction (C_l , C_m and C_h respectively) as the maximum cloud fraction between the surface
114 and 780 hPa, 780 and 440 hPa, and 440 and 50 hPa, respectively. Although previous studies assessed C_l by
115 maximum cloud fraction between the surface and 680 hPa (Noda and Satoh 2014; Zhou et al. 2016), we selected
116 the boundary of 780 hPa to emphasize the response of marine boundary-layer cloud over cool oceans (e.g. Norris
117 1998; Luo et al. 2016). Note that ΔC_l is not sensitive to choices of upper boundary criterion (e.g. 680 hPa or 800
118 hPa) because the near-surface (below 850 hPa level) response dominates the low cloud adjustment (see sect. 3.1).

119

120 **2.2. AMIP simulations with prescribed land surface temperature**

121 In addition to CMIP5 model ensemble, we use the results of prescribed land surface temperature simulations
122 conducted in an AGCM, ACCESS1.0 (Bi et al. 2013; Frauen et al. 2014). Details of model configuration and
123 experimental setup are found in Ackerley and Dommenges (2016) and Ackerley et al. (2018). Simulated data are
124 available from Ackerley (2017). Here we briefly describe the experimental framework and decomposition methods.
125 ACCESS is configured similarly to the Hadley Centre Global Environmental Model version 2 (HadGEM2; Martin
126 et al. 2011). The version of ACCESS1.0 used here has a horizontal resolution of 3.75° longitude and 2.5° latitude
127 and 38 vertical levels. The timestep of the model integration is 30 minutes. The AGCM includes physics
128 parameterizations (precipitation, cloud, convection, radiative transfer, boundary layer and aerosols) and is coupled

129 with a land surface parameterization (Cox et al. 1999; Essery et al. 2001). Soil moisture and temperature are
130 simulated over four vertical layers (0.1, 0.25, 0.65 and 2 m depth).

131 To examine physical mechanisms responsible for rapid adjustment, we use AGCM runs with free-varying
132 land condition (free runs) and prescribed land surface temperature experiments (PL runs). All the simulations are
133 driven by observed SST and sea ice fraction from 1979 to 2008. In this study, the climatology of the last 25 years
134 out of the 30-yr integration is examined. Free runs with CO₂ concentrations of 346 and 1384 ppmv are referred as
135 A and A4x, respectively. Here prescribed SST is not identical to that used in CMIP5 sstClim run (model
136 climatology; sect. 2.1), but the SST difference doesn't substantially affect results of this study (not shown). In
137 A4xrad, the radiation code uses CO₂ concentration of 1384 ppmv but the vegetation uses 346 ppmv in order to
138 isolate the effect of the plant physiological response (Boucher et al. 2009; Doutriaux-Boucher et al. 2009).
139 Instantaneous values of the surface temperature, soil temperature and moisture (on each soil level) in these runs
140 are stored every three hours. In the PL runs, the stored land conditions are read in by the model every three hours
141 and updated (by interpolation) every hour. In A4xrad_{PL} run, for example, land surface conditions are replaced by
142 those simulated in A run but only the radiation code refers to a CO₂ concentration of 1384 ppmv. If we compare
143 the results of A4xrad_{PL} and A_{PL} runs, the difference indicates the effect of atmospheric radiative heating rate due
144 to CO₂ quadrupling without any effects of perturbations in land conditions (RAD_ATM; Table 1). Similarly, the
145 effect of the plant physiological response (PLANT), the effect of land warming due to atmospheric radiative
146 perturbation (RAD_LAND), and a residual (RES) are calculated by comparing free and PL runs (Table 1; see also
147 Fig. S1). Note that interpolated land surface conditions are updated every hour instead of every 30 minutes (the

148 timestep of model integrations). Therefore, the results of PL runs are not strictly identical to free runs (see Ackerley
149 et al. 2018 for detail). We checked the residual term due to this difference, but it does not affect our results
150 substantially (see Figs. S2, S3 and Supplementary Discussion).

151

152 **3. Seasonality in cloud adjustment in CMIP5 models**

153 We first examine the robustness of cloud adjustments and its seasonal variation across CMIP5 models.
154 Figure 1a–c shows the 15-model ensemble mean of annual-mean cloud adjustment over the ocean. As
155 demonstrated in previous studies (Kamae and Watanabe 2012; Zelinka et al. 2013; Vial et al. 2013; Kamae et al.
156 2015), global-mean total cloud amount tends to decrease (with weak increase over several regions including the
157 North Pacific; Fig. 1a), leading to an enhancement of effective radiative forcing of CO₂ via reduction of shortwave
158 reflection due to clouds. Kamae and Watanabe (2013) concluded that this anomalous shortwave component of
159 cloud radiative effect is due to low cloud reduction from simulations based on an AGCM. However, if we
160 decompose the multi-model cloud adjustment into different vertical levels (sect. 2.1), it is clearly found that the
161 annual-mean cloud reduction dominates in the middle and upper troposphere rather than the lower troposphere
162 (Fig. 1b, c). The model-simulated cloud fraction below the 780 hPa level is increased over subtropical low cloud
163 regions, including California and the Canary Islands, and the extratropical Northern Hemisphere. The 27 °C SST
164 isotherm is shown in these panels as an approximation of the boundary between tropical deep convective region
165 and subtropical atmospheric subsidence regions (Zhang 1993; Sud et al. 1999). In contrast to the anomalous low
166 cloud cover over the subtropics, such cloud adjustments are not consistently found in the total cloud amount in the

167 subtropics (Fig. 1a), suggesting greater contributions from middle and high clouds than low cloud. The increase
168 in low-cloud cover in annual-mean field is clearly found over cool SST ($< 27\text{ }^{\circ}\text{C}$) regions over the Northern
169 Hemisphere but is not apparent over the Southern Hemisphere (Fig. 1c).

170 In the fixed-SST increased- CO_2 simulations, changes in boundary-layer inversion strength is a major factor
171 for the low cloud response (Klein and Hartmann 1993; Qu et al. 2015b; Myers and Norris 2016; Kawai et al. 2017).
172 Figure 2 shows anomalies in SAT, air temperature at the 700 hPa level (T_{700}), and estimated inversion strength
173 (EIS; Wood and Bretherton 2006) in response to quadrupling CO_2 . Here a given EIS response (ΔEIS) can be
174 approximated by a linear combination of ΔSAT and ΔT_{700} (see Qu et al. 2014, 2015a for detail). In the fixed-SST
175 simulations, ΔT_{700} dominates ΔEIS because of little ΔSAT (Fig. 2). In response to increasing CO_2 , the lower
176 troposphere warms up through radiative heating due to instantaneous CO_2 radiative forcing (e.g. Sugi and
177 Yoshimura 2004; Collins et al. 2006; Kamae and Watanabe 2013) and the effect of land warming (e.g. Chadwick
178 et al. 2014; Kamae et al. 2014), resulting in positive ΔEIS over ocean (Webb et al. 2013; Qu et al. 2015a). This
179 enhanced inversion is especially dominant over the extratropical North Pacific and subtropical low-cloud regions
180 (off the coasts of California and the Canary Islands; Fig. 2c) but relatively weak over warm oceans (see SST
181 contours in Fig. 1c), consistent with ΔC_1 (Fig. 1c). Table 2 summarizes area-averaged ΔC and ΔEIS . In contrast to
182 strong and robust reductions of C_h and C_m (and resultant C_t), annual-mean C_1 shows increases (no changes) over
183 the low-cloud regions (cool ocean) with large inter-model spreads (see Figs. S4, S5 and S6).

184 The weak annual-mean ΔC_1 can be understood as a result of seasonal compensation. Figure 1d–i show
185 wintertime and summertime cloud adjustment. Here winter (summer) is determined by November-to-March mean

186 and May-to-September mean over the Northern (Southern) and Southern (Northern) Hemispheres, respectively.

187 While $\Delta C_h + \Delta C_m$ is largely consistent between the two seasons (reduction over extratropics; Fig. 1e, h), CMIP5

188 models consistently show clear seasonality in the low cloud adjustment: general decrease in winter but greater

189 increases over the subtropics and extratropics in summer (Figs. 1f, i, S6). The large increase in the summertime

190 Northern Hemisphere is also found in the total cloud adjustment (Fig. 1g), contributing to the increase in C_t in

191 some regions in the annual-mean field (Fig. 1a). The effect of ΔC_l on ΔC_t suggests an important contribution to

192 radiative balance at TOA (i.e. effective radiative forcing). Table 3 summarizes seasonal variation in the response

193 of the shortwave cloud radiative effect (SWcld) to quadrupling CO_2 in CMIP5 models. Here, SWcld is simply

194 calculated by taking the difference between all-sky radiation and clear-sky radiation at TOA that includes the cloud

195 masking effect (Soden et al. 2004, 2008). Note that the cloud masking effect on the shortwave component of cloud

196 adjustment is much smaller than that on the longwave component (Wyant et al. 2012; Kamae et al. 2015). Positive

197 ΔSWcld is consistently simulated in 15 models in all seasons. Over cool oceans, summertime ΔSWcld is weaker

198 than that in winter, consistent with summertime increment of C_l (and seasonal variation of ΔC_l) over the subtropics

199 and extratropics (Fig. 1i). However, the effects of seasonally-variant ΔC_l on ΔC_t and ΔSWcld are relatively limited

200 compared to those of ΔC_h and ΔC_m (Tables 2, 3, Fig. 1).

201 Figure 3 compares zonal-mean ΔEIS and ΔC_l averaged over cool oceans ($\text{SST} < 27^\circ \text{C}$). In contrast to small

202 or negative ΔC_l during winter, summertime positive ΔC_l is consistently found in 15 CMIP5 models (Table 2, Figs.

203 1i, 3b, S6). The seasonal variation (summertime enhancement) is also consistently found in ΔEIS (Table 2, Figs.

204 2f, i, 3a) and ΔT_{700} (Fig. 2e, h), and is larger over the Northern Hemisphere than the Southern Hemisphere. Possible

205 reasons for the seasonal variations in temperature and ΔEIS and their interhemispheric differences are discussed
206 in the next section. Seasonal variation (summer minus winter) in ΔEIS and ΔC_1 shown in Fig. 4 is closely related
207 each other: neutral or partly negative over the tropics ($20^\circ S$ – $20^\circ N$) but positive and large over subtropics and
208 extratropics especially over the North Pacific and low cloud regions off the coasts of California and the Canary
209 Islands. This spatial coherence (correlation coefficient is 0.56) indicates that the seasonal variation in ΔC_1 is largely
210 controlled by that in lower tropospheric warming (and resultant ΔEIS).

211

212 **4. Decomposition of cloud adjustment**

213 In the previous section, we demonstrated that low cloud adjustment over cool oceans exhibits a seasonal
214 reversal and is consistently found among CMIP5 models. The summertime increase in C_1 is likely to be related to
215 summertime enhancement of lower tropospheric warming and resultant positive ΔEIS . From Fig. 2, larger land
216 surface warming during summer than winter is a possible reason for the seasonal variations in lower tropospheric
217 temperature and C_1 . To examine physical mechanisms in detail, we further use outputs from prescribed land surface
218 temperature experiments conducted in ACCESS1.0 (sect. 2.2). Before we decompose the cloud adjustment, we
219 compare adjustments of temperature, EIS and cloud fraction in this model with results from the CMIP5 ensemble.
220 Figure 5 shows annual-mean cloud adjustment and temperature response. Table 4 summarizes annual-mean
221 responses averaged over cool oceans. As found in CMIP5 models (Figs. 1, 2), the land surface and lower
222 troposphere warm up in response to increasing CO_2 , resulting in a general increase in EIS (Table 4) especially over
223 the subtropics and extratropics (Fig. 5a–c). The enhanced EIS is consistent with increased C_1 over cool oceans, in

224 contrast to large decreases in C_h and C_m (Table 4, Fig. 5e, f). The C_l increase simulated in ACCESS1.0 is generally
225 larger than CMIP5 multi-model mean (Tables 2, 4). Among CMIP5 models, both the strength and spatial pattern
226 of ΔC_l exhibit large inter-model spreads (Table 3, Fig. 3b; see Fig. S5). However, increased C_l in the North Pacific
227 (and other regions with large low-cloud fractions) and their seasonal variations found in CMIP5 models (Figs. 1,
228 3) are consistently simulated in ACCESS1.0 (Fig. 5; detailed below). Thus, we examine the physical mechanisms
229 responsible for the seasonal variation of C_l adjustment by using the sensitivity simulations conducted in this model.

230 Figures 6 and 7 show decompositions of C_l , C_m and C_h adjustment to quadrupling CO_2 based on
231 ACCESS1.0 sensitivity simulations detailed in sect. 2.2. The increase in annual-mean C_l (Fig. 5f) is almost entirely
232 explained by the sum of two comparable contributions: RAD_ATM and RAD_LAND effects (Fig. 6a, c; see Table
233 1). The effect of RAD_ATM results in a general increase in C_l over cool oceans in both hemispheres, while the
234 RAD_LAND effect is more dominant over the Northern Hemisphere than the Southern Hemisphere. It should also
235 be noted that effects of RES on ΔC_l and $\Delta C_h + \Delta C_m$ are not negligible (sect. 2.2; Figs. S2, S3; see Supplementary
236 Discussion). The characteristics of effects of RAD_ATM and RAD_LAND are consistent with ΔEIS shown in Fig.
237 8. In response to increasing CO_2 , the perturbation in longwave radiative heating rate due to instantaneous radiative
238 forcing warms the lower-to-upper troposphere (Kamae and Watanabe 2013; Ogura et al. 2014) with its peak at the
239 700–850 hPa level (Sugi and Yoshimura 2004; Collins et al. 2006). The radiative heating results in enhanced lower
240 tropospheric stability over most of the oceans (Fig. 8a). Possible reasons for spatial pattern of the lower-
241 tropospheric warming are discussed in sect. 5. The effect of RAD_LAND, in contrast, is strongest over the
242 subtropics and extratropics (especially over the North Pacific; Fig. 8c) with its peak at middle and upper

243 troposphere (not shown). The stronger effect of RAD_ATM than RAD_LAND over the subtropics and extratropics
244 is consistent with relative strength of their effects on C_1 (Fig. 6a, c). The enhanced stability over the subtropics and
245 extratropics (Figs. 2c, 5c) can be understood as a result of a combined effect of RAD_ATM and RAD_LAND. The
246 effect of PLANT negatively contributes to the responses of EIS and C_1 (Figs. 6b, 8b), which resulted from changes
247 in land surface heat and moisture budgets. The stomatal closure from higher CO_2 concentration causes a decrease
248 in evapotranspiration, an increase in the sensible heat flux, and surface warming over tropical land (e.g. Dong et
249 al. 2009; Andrews and Ringer 2014; DeAngelis et al. 2016). The land surface warming in addition to the decreased
250 evapotranspiration partly affects EIS (Dong et al. 2009) and C_1 over ocean; however, the total contributions of
251 PLANT are minor compared to RAD_ATM and RAD_LAND (Table 4, Fig. S2a, c; see Supplementary Discussion).

252 Which effect dominates the seasonal variation in cloud adjustment? To answer this question, we examine
253 wintertime and summertime temperature and C_1 adjustment. As shown in Fig. 9, both RAD_ATM and
254 RAD_LAND effects act to warm the lower troposphere both in winter and summer (Fig. 9a, d, g, j). However,
255 wintertime warming is generally weaker than that during summer, resulting in seasonal variations in ΔEIS and ΔC_1
256 (Fig. 9b, c, e, f, h, i, k, l). Both RAD_ATM and RAD_LAND effects result in positive ΔC_1 due to large positive
257 ΔC_1 during summer, in contrast to small positive ΔC_1 during winter (Table 4). Note that the sign and magnitude of
258 ΔC_t , $\Delta C_h + \Delta C_m$, and ΔC_1 simulated in ACCESS1.0 (e.g. wintertime positive ΔC_1 over the Southern Hemisphere
259 middle latitude; Fig. S7f) are partly different from CMIP5 multi-model mean (Tables 2, 3, 4, Figs. 1, 2, 5d–f) but
260 seasonal contrasts (summer minus winter) in ΔSAT , ΔT_{700} , ΔEIS , and ΔC_1 are generally consistent with the model
261 ensemble mean (see Figs. S7, S8). Figure 10 compares seasonal-mean zonal-mean adjustments due to the effects

262 of RAD_ATM and RAD_LAND. Both effects result in strong warming in summer over the subtropics and
263 extratropics with its peak over 50°S–40°S and 40°N–50°N (Fig. 10a, c). Seasonal ΔC_1 is rather noisy compared to
264 ΔEIS , but seasonal contrasts are similarly found (Fig. 10b, d) and are consistent with the total adjustment simulated
265 in CMIP5 models (Fig. 3). Seasonal contrasts in ΔC_1 and ΔEIS due to the RAD_LAND effect are consistently
266 larger over the Northern Hemisphere than the Southern Hemisphere (Fig. 10c, d). Such interhemispheric
267 differences can also be found in CMIP5 ensemble (Fig. 3), suggesting that the stronger low cloud adjustments over
268 the Northern Hemisphere than the Southern Hemisphere are attributed to the land effect.

269

270 **5. Possible reasons for the seasonal variation**

271 The low-cloud adjustment consistently dominates during summer among the CMIP5 models. Sensitivity
272 tests using ACCESS1.0 indicate that the seasonally-variant low-cloud adjustment can be attributed to seasonality
273 in the response of inversion strength to increasing CO₂, which itself is a response to both through atmospheric
274 radiative perturbation and radiative land warming. A remaining question addressed here is: what is the physical
275 reason for the seasonal difference in lower tropospheric warming despite seasonally-uniform CO₂ increments?
276 One possible factor is a dynamic contribution: the effect of atmospheric circulation response to increasing CO₂.
277 Bony et al. (2013) suggested that CO₂ forcing may slow the tropical atmospheric circulation including Hadley and
278 Walker circulations because CO₂-induced longwave heating (weakened radiative cooling; e.g. Sugi and Yoshimura
279 2004; Collins et al. 2006) especially over dry subsiding regions possibly change the tropical overturning circulation
280 strength. Merlis (2015) further showed that clear-sky CO₂ forcing reduces tropical atmospheric circulation

281 intensity via reduction of radiative cooling. Such changes in large-scale atmospheric circulation possibly result in
282 tropospheric temperature changes through vertical advection and adiabatic compression.

283 Figure 11 shows the response of vertical temperature advection and adiabatic compression to quadrupling
284 CO₂ via RAD_ATM effect. Changes in vertical pressure velocity at the 700 hPa level ($\Delta\omega_{700}$) are generally opposite
285 to the climatological ω_{700} (Fig. 11a, c), indicating the weakening of atmospheric circulation. Over convective
286 regions, positive $\Delta\omega_{700}$ (anomalous subsidence) are consistently found over the both hemispheres. The anomalous
287 subsidence results in warming (warm advection) because potential temperature is larger at higher altitude than
288 lower altitude. Inversely, a cooling effect dominates over climatological subsidence regions including off the coasts
289 of California and the Canary Islands, as a result of anomalous ascending motion (Fig. 11b, d). These spatial patterns
290 and zonal-mean heating rate (Fig. 11e) are not similar to those in lower-tropospheric warming and ΔEIS resulted
291 from the RAD_ATM effect (Figs. 9, 10).

292 Another possible factor is seasonality in CO₂ instantaneous radiative forcing. Huang et al. (2016) revealed
293 that instantaneous radiative forcing of spatially uniform increment of CO₂ is not spatially uniform because of
294 spatial patterns of (1) surface temperature, (2) upper-level (10 hPa) atmospheric temperature, and (3) column water
295 vapor content. Similarly, instantaneous radiative forcing could be seasonally non-uniform. To test this point, we
296 examine instantaneous radiative forcing of CO₂ provided by five climate models: CanAM4, HadGEM2-A, IPSL-
297 CM5A-LR, MIROC3, and MIROC5. Although this diagnostic is not available for ACCESS1.0, spatial patterns
298 and seasonal variation in this model are likely to be very similar to those in HadGEM2-A, due to the almost
299 identical model formulation (see sect. 2.2). Figure 12 compares the simulated radiative (shortwave and longwave)

300 heating at the 700 hPa level due to instantaneous CO₂ forcing between the two seasons. Instantaneous radiative
301 forcing is stronger over lower latitudes than higher latitudes because higher SAT results in stronger forcing (Huang
302 et al. 2016). In addition, instantaneous radiative forcing over ITCZ is weaker than surrounding subtropical regions
303 because of more water vapor content (Merlis 2015). These two factors also determine the seasonal variation in
304 instantaneous radiative forcing. The climate models examined here consistently show stronger radiative heating
305 over the subtropics and extratropics (except for the eastern tropical Pacific in MIROC5 model) during summer
306 than winter (Fig. 12). Note that instantaneous radiative forcing simulated in MIROC3 is distinct from other models
307 due to difference in the radiative calculation as reported in Ogura et al. (2014). Except for the wet convective
308 regions (SST > 27 °C), the summertime heating rate over cool oceans is stronger than winter, consistent with
309 stronger ΔT_{700} and ΔEIS (Fig. 9). The stronger heating rate is consistent with higher SAT during summer than
310 winter. In the fixed-SST simulations, SAT should be higher during summer than winter due to higher SST and
311 seasonal variation in incoming solar radiation. As a result, seasonal variations in SAT, instantaneous radiative
312 forcing, ΔT_{700} , ΔEIS , and ΔC_1 (stronger instantaneous radiative forcing during summer results in larger increase in
313 C_1 than winter) should be consistent among different climate models (Figs. 1, 2, 12, S6). Note that near-surface
314 instantaneous radiative forcing is also perturbed due to increased CO₂ (figure not shown), but prescribed SST
315 damps the near-surface temperature response to radiation (Fig. 1g–i), resulting in the dominant contribution of the
316 radiative heating at the 700 hPa level (Fig. 12) to ΔEIS (Figs. 8–10).

317

318 **6. Summary and discussions**

319 Multiple climate models consistently simulate increased low cloud over the subtropics and extratropics in
320 the Northern Hemisphere in the rapid adjustment to increasing CO₂ in contrast to largest decreases in middle and
321 high clouds. In response to CO₂ forcing, reduced radiative cooling in the lower troposphere together with land
322 surface warming induces lower tropospheric warming, resulting in enhanced inversion strength of the boundary
323 layer and increased low cloud over cool oceans. The enhanced inversion strength and low cloud increase are
324 consistently amplified during summer in the both hemispheres. By examining a set of prescribed land surface
325 temperature experiments in an AGCM, the effects of atmospheric radiative heating, radiative land warming, the
326 plant physiological response, and residual term of the low cloud adjustment are evaluated. The effects of
327 atmospheric radiative heating and radiative land warming are comparably important for the low cloud adjustment
328 over cool oceans. During summer, higher climatological SAT results in stronger instantaneous radiative forcing of
329 CO₂ than winter despite a seasonally-constant increment of CO₂ concentration. As a result, radiative warming of
330 the lower troposphere and land surface are amplified during summer, resulting in a stronger enhancement of
331 inversion strength and low-cloud increase over ocean than in winter. The present study relates seasonal variations
332 in climatological SAT, EIS adjustment, and low-cloud adjustment.

333 The results of the present study, especially seasonal variation in low-cloud adjustment over wide oceanic
334 area, have implications for climate sensitivity. In most previous studies on cloud adjustment and climate sensitivity,
335 the response of cloud cover was examined in the annual mean. This averaging procedure doesn't matter for the
336 tropics, in which the seasonal cycle doesn't dominate. Over the subtropics and extratropics, in contrast, incoming
337 solar radiation exhibits large seasonal variation (seasonal-mean insolation is 424 W m⁻² in May-to-September and

338 243 W m⁻² in November-to-March in EQ–90°N average). Over these regions, large seasonal variations can also
339 be found in climatological SAT, atmospheric circulation, and cloud cover. The seasonal reversal of climatological
340 atmospheric circulation and associated variations in precipitation and cloud cover are very important when we try
341 to understand physical mechanisms responsible for their responses to external forcing. For example, their response
342 to climate warming over tropical-to-subtropical land regions are substantially controlled by climatological
343 monsoon circulations (Kamae et al. 2016b). The results of the present study imply that we need to examine the
344 seasonal dependence of cloud feedbacks (e.g. Colman 2003; Taylor et al. 2011) over the subtropics and extratropics
345 to external forcing as well as cloud adjustment. Chung and Soden (2018) identified that inter-model spreads of
346 cloud adjustment and feedback are significantly anticorrelated through marine boundary-layer clouds. It should
347 also be noted that rapid adjustments of cloud optical depth in addition to cloud fraction were also suggested as
348 important factors for the total spread of cloud adjustment among climate models (Zelinka et al. 2013). Further
349 investigations focused on seasonal variations in cloud adjustment and feedback, their relationship, and underlying
350 physical mechanisms may improve our understanding of uncertainty and possible constraints on climate sensitivity.

351

352 **Acknowledgements**

353 We acknowledge the World Climate Research Programme’s Working Group on Coupled Modeling, which
354 is responsible for CMIP, and we thank the climate modeling groups (listed in Table S1 in the online supplement)
355 for producing and making available their model output. For CMIP5, the US Department of Energy's Program for
356 Climate Model Diagnosis and Intercomparison provided coordinating support, and led the development of the

357 software infrastructure in partnership with the Global Organization for Earth System Science Portals. This work
358 was supported by JSPS KAKENHI Grant Numbers 17K14388 and 17K05657, and the Integrated Research
359 Program for Advancing Climate Models (TOUGOU program) from the Ministry of Education, Culture, Sports,
360 Science and Technology (MEXT), Japan. We would like to acknowledge M. Watanabe and H. Shiogama for helpful
361 discussions.

362

363 **References**

- 364 Abe M, Shiogama H, Yokohata T, Emori S, Nozawa T (2015) Asymmetric impact of the physiological effect of
365 carbon dioxide on hydrological responses to instantaneous negative and positive CO₂ forcing. *Clim Dyn*
366 45:2181–2192
- 367 Ackerley D (2017) AMIP ACCESS 1.0 prescribed land experiment collection v1.0: PLAMIP. NCI National
368 Research Data Collection, [https://researchdata.andc.org.au/prescribed-land-amip-experiments-](https://researchdata.andc.org.au/prescribed-land-amip-experiments-collection/940117)
369 [collection/940117, https://doi.org/10.4225/41/59521137d6c42](https://doi.org/10.4225/41/59521137d6c42) , accessed: 15-03-2018.
- 370 Ackerley D, Dommenges D (2016) Atmosphere-only GCM (ACCESS1.0) simulations with prescribed land surface
371 5 temperatures. *Geosci Model Dev* 9:2077–2098
- 372 Ackerley D, Chadwick R, Dommenges E, Petrelli P (2018) An ensemble of AMIP simulations with prescribed land
373 surface temperatures. *Geosci Model Dev Discuss*. doi:10.5194/gmd-2018-77
- 374 Andrews T, Ringer MA (2014) Cloud feedbacks, rapid adjustments, and the forcing-response relationship in a
375 transient CO₂ reversibility scenario. *J Clim* 27:1799–1818
- 376 Andrews T, Gregory JM, Forster PM, Webb MJ (2012) Cloud adjustment and its role in CO₂ radiative forcing and
377 climate sensitivity: A review. *Surv Geophys* 33:619–635
- 378 Bi D, Dix M, Marsland SJ, et al. (2013) The ACCESS coupled model: description, control climate and evaluation.
379 *Aust Meteorol Ocean J* 63:41–64
- 380 Blossey PN, Bretherton CS, Cheng A, Endo S, Heus T, Lock AP, van der Dussen JJ (2016) CGILS Phase 2 LES
381 intercomparison of response of subtropical marine low cloud regimes to CO₂ quadrupling and a CMIP3
382 composite forcing change. *J Adv Model Earth Syst* 8:1714–1726
- 383 Boucher O, Jones A, Betts RA (2009) Climate response to the physiological impact of carbon dioxide on plants in
384 the Met Office Unified Model HadCM3. *Clim Dyn* 32:237–249

385 Bretherton CS (2015) Insights into low-latitude cloud feedbacks from high-resolution models. *Phil Trans R Soc A*
386 373:3354–3360

387 Bretherton CS, Blossey PN, Jones CR (2013) Mechanisms of marine low cloud sensitivity to idealized climate
388 perturbations: A single-LES exploration extending the CGILS cases. *J Adv Model Earth Syst* 5:316–337

389 Bretherton CS, Blossey PN, Stan C (2014) Cloud feedbacks on greenhouse warming in the superparameterized
390 climate model SP-CCSM4. *J Adv Model Earth Syst* 6:1185–1204

391 Bony S, Bellon G, Klocke D, Sherwood S, Fermepin S, Denvil S (2013) Robust direct effect of carbon dioxide on
392 tropical circulation and regional precipitation. *Nat Geosci* 6:447–451

393 Boucher O, Randall D, Artaxo P, et al (2014) Clouds and aerosols. In: Stocker TF, editor. *Climate change 2013:*
394 *the physical science basis. Contribution of working group I to the Fifth Assessment Report of the*
395 *Intergovernmental Panel on Climate Change. Cambridge: Cambridge University Press, p. 571–658*

396 Ceppi P, Briant F, Zelinka MD, Hartmann DL (2017) Cloud feedback mechanisms and their representation in
397 global climate models. *WIREs Clim Change* 8:e465. doi:10.1002/wcc.465

398 Cess RD, Potter GL, Blanchet J (1989) Interpretation of cloud-climate feedback as produced by 14 atmospheric
399 general circulation models. *Science* 245:513–516

400 Chadwick R, Good P, Andrews T, Martin G (2014) Surface warming patterns drive tropical rainfall pattern
401 responses to CO₂ forcing on all timescales. *Geophys Res Lett* 41:610–615

402 Chadwick R, Ackerley D, Ogura T, and Dommenges D (2018) Separating the influences of land warming, the
403 direct CO₂ effect, the plant physiological effect and SST warming on regional precipitation and circulation
404 changes. *J Geophys Res Atmos* (submitted)

405 Chen J, Bordoni S (2016) Early summer response of the East Asian Summer Monsoon to atmospheric CO₂ forcing
406 and subsequent sea surface warming. *J Clim* 29:5431–5446

407 Chung E-S, Soden BJ (2018) On the compensation between cloud feedback and cloud adjustment in climate
408 models. *Clim Dyn* 50:1267–1276

409 Collins WD, Ramaswamy V, Schwarzkopf MD et al (2006) Radiative forcing by well-mixed greenhouse gases:
410 estimates from climate models in the Intergovernmental Panel on Climate Change (IPCC) fourth assessment
411 report (AR4). *J Geophys Res* 111:D14317. doi:10.1029/2005JD006713

412 Colman R (2003) Seasonal contributions to climate feedbacks. *Clim Dyn* 20:825–841

413 Colman RA, McAvaney BJ (2011) On tropospheric adjustment to forcing and climate feedbacks. *Clim Dyn*
414 36:1649–1658

415 Cox PM, Betts RA, Bunton CB, Essery RLH, Rowntree PR, Smith J (1999) The impact of new land surface physics
416 on the GCM simulation of climate and climate sensitivity. *Clim Dyn* 15:183–203

417 DeAngelis AM, Qu X, Hall A (2016) Importance of vegetation processes for model spread in the fast precipitation
418 response to CO₂ forcing. *Geophys Res Lett* 43:12550–12559

419 Dong B, Gregory JM, Sutton RT (2009) Understanding land–sea warming contrast in response to increasing
420 greenhouse gases. Part I: transient adjustment. *J Clim* 22:3079–3097

421 Doutriaux-Boucher M, Webb MJ, Gregory JM, Boucher O (2009) Carbon dioxide induced stomatal closure
422 increases radiative forcing via a rapid reduction in low cloud. *Geophys Res Lett* 36:L02703.
423 doi:10.1029/2008GL036273

424 Essery R, Best MJ, Cox PM (2001) Hadley Centre Technical Note 30: MOSES2.2 technical documentation, Tech.
425 rep., United Kingdom Met Office,
426 <https://digital.nmla.metoffice.gov.uk/file/sdb%3AdigitalFile%7Cd5dbe569-5ef7-41c8-b55b-3b63dff5afbe/>

427 Frauen C, Dommenges D, Tyrrell N, Rezný M, Wales S (2014) Analysis of the nonlinearity of El Niño Southern
428 Oscillation teleconnections. *J Clim* 27:6225–6244

429 Gregory JM, Webb MJ (2008) Tropospheric adjustment induces a cloud component in CO₂ forcing. *J Clim* 21:58–
430 71

431 Hansen J et al (2002) Climate forcings in Goddard Institute for Space Studies SI2000 simulations. *J Geophys Res*
432 107:4347. doi:10.1029/2001JD001143

433 He J, Soden BJ (2015) Anthropogenic weakening of the tropical circulation: the relative roles of direct CO₂ forcing
434 and sea surface temperature change. *J Clim* 28:8728–8742

435 He J, Soden BJ (2016) A re-examination of the projected subtropical precipitation decline. *Nat Clim Change* 7:53–
436 57

437 Huang Y, Tan X, Xia Y (2016) Inhomogeneous radiative forcing of homogeneous greenhouse gases. *J Geophys*
438 *Res Atmos* 121:2780–2789

439 Kamae Y, Watanabe M (2012) On the robustness of tropospheric adjustment in CMIP5 models. *Geophys Res Lett*
440 39:L23808. doi:10.1029/2012GL054275

441 Kamae Y, Watanabe M (2013) Tropospheric adjustment to increasing CO₂: its timescale and the role of land–sea
442 contrast. *Clim Dyn* 41:3007–3024

443 Kamae Y, Watanabe M, Kimoto M, Shiogama H (2014) Summertime land–sea thermal contrast and atmospheric
444 circulation over East Asia in a warming climate–Part II: Importance of CO₂-induced continental warming.
445 *Clim Dyn* 43:2569–2583

446 Kamae Y, Watanabe M, Ogura T, Yoshimori M, Shiogama H (2015) Rapid adjustments of cloud and hydrological
447 cycle to increasing CO₂: a review. *Curr Clim Change Rep* 1:103–113

448 Kamae Y, Ogura T, Shiogama H, Watanabe M (2016a) Recent progress toward reducing the uncertainty in tropical
449 low cloud feedback and climate sensitivity: a review. *Geosci Lett* 3:17. doi:10.1186/s40562-016-0053-4

450 Kamae Y, Ogura T, Watanabe M, Xie S-P, Ueda H (2016b) Robust cloud feedback over tropical land in a warming
451 climate. *J Geophys Res Atmos* 121:2593–2609

452 Kawai H, Koshiro T, Webb MJ (2017) Interpretation of factors controlling low cloud cover and low cloud feedback
453 using a unified predictive index. *J Clim* 30:9119–9131

454 Klein SA, Hartmann DL (1993) The seasonal cycle of low stratiform clouds. *J Clim* 6:1587–1606

455 Luo T, Wang Z, Zhang D, Chen B (2016) Marine boundary layer structure as observed by A-train satellites. *Atmos*
456 *Chem Phys* 16:5891–5903

457 The HadGEM2 Development Team: Martin GM, Bellouin N, Collins WJ, et al. (2011) The HadGEM2 family of
458 Met Office Unified Model climate configurations. *Geosci Model Dev* 4:723–757

459 Merlis TM (2015) Direct weakening of tropical circulations from masked CO₂ radiative forcing. *Proc Natl Acad*
460 *Sci USA* 112:13167–13171

461 Myers TA, Norris JR (2016) Reducing the uncertainty in subtropical cloud feedback. *Geophys Res Lett* 43: 2144–
462 2148

463 Noda AT, Satoh M (2014) Intermodel variances of subtropical stratocumulus environments simulated in CMIP5
464 models. *Geophys Res Lett* 41:7754–7761

465 Norris JR (1998) Low cloud type over the ocean from surface observations. Part I: relationship to surface
466 meteorology and the vertical distribution of temperature and moisture. *J Clim* 11:369–382

467 Ogura T, Webb MJ, Watanabe M, Lambert FH, Tsushima Y, Sekiguchi M (2014) Importance of instantaneous
468 radiative forcing for rapid tropospheric adjustment. *Clim Dyn* 43:1409–1421

469 Qu X, Hall A, Klein SA, Caldwell PM (2014) On the spread of changes in marine low cloud cover in climate
470 model simulations of the 21st century. *Clim Dyn* 42:2603–2626

471 Qu X, Hall A, Klein SA, Caldwell PM (2015a) The strength of the tropical inversion and its response to climate
472 change in 18 CMIP5 models. *Clim Dyn* 45:375–396

473 Qu X, Hall A, Klein SA, DeAngelis AM (2015b) Positive tropical marine low-cloud cover feedback inferred from
474 cloud-controlling factors. *Geophys Res Lett* 42:7767–7775

475 Ringer MA, Andrews T, Webb MJ (2014) Global-mean radiative feedbacks and forcing in atmosphere-only and
476 fully-coupled climate change experiments. *Geophys Res Lett* 41:4035–4042

477 Shaw TA, Voigt A (2015) Tug of war on summertime circulation between radiative forcing and sea surface
478 warming. *Nat Geosci* 8:560–566

479 Shaw TA, Voigt A (2016) Land dominates the regional response to CO₂ direct radiative forcing. *Geophys Res Lett*
480 43:11383–11391

481 Sherwood SC, Bony S, Boucher O, Bretherton C, Forster PM, Gregory JM, Stevens B (2015) Adjustments in the
482 forcing-feedback framework for understanding climate change. *Bull Am Meteorol Soc* 96:217–228

483 Shine KP, Cook J, Highwood EJ, Joshi MM (2003) An alternative to radiative forcing for estimating the relative
484 importance of climate change mechanisms. *Geophys Res Lett* 30:2047. doi:10.1029/2003GL018141

485 Shiogama H, Watanabe M, Yoshimori M, et al (2012) Perturbed physics ensemble using the MIROC5 coupled
486 atmosphere-ocean GCM without flux corrections: experimental design and results. *Clim Dyn* 39:3041–3056

487 Soden BJ, Broccoli AJ, Hemler RS (2004) On the use of cloud forcing to estimate cloud feedback. *J Clim* 17:3661–
488 3665

489 Soden BJ, Held IM, Colman R, Shell KM, Kiehl JT, Shields CA (2008) Quantifying climate feedbacks using
490 radiative kernels. *J Clim* 21:3504–3520

491 Sud YC, Walker GF, Lau KM (1999) Mechanisms regulating sea-surface temperatures and deep convection in the
492 tropics. *Geophys Res Lett* 26:1019–1022

493 Sugi M, Yoshimura J (2004) A mechanism of tropical precipitation change due to CO₂ increase. *J Clim* 17:238–
494 243

495 Taylor PC, Ellingson RG, Cai M (2011) Seasonal variations of climate feedbacks in the NCAR CCSM3. *J Clim*
496 24:3433–3444

497 Taylor KE, Stouffer RJ, Meehl GA (2012) An overview of CMIP5 and the experiment design. *Bull Am Meteorol*
498 *Soc* 93:485–498

499 Vial J, Dufresne J-L, Bony S (2013) On the interpretation of inter-model spread in CMIP5 climate sensitivity
500 estimates. *Clim Dyn* 41:3339–3362

501 Watanabe M, Shiogama H, Yoshimori M, Ogura T, Yokohata T, Okamoto H, Emori S, Kimoto M (2012) Fast and
502 slow timescales in the tropical lowcloud response to increasing CO₂ in two climate models. *Clim Dyn*
503 39:1627–1641

504 Webb MJ, Lambert FH, Gregory JM (2013) Origins of differences in climate sensitivity, forcing and feedback in
505 climate models. *Clim Dyn* 40:677–707

506 Wood R, Bretherton CS (2006) On the relationship between stratiform low cloud cover and lower-tropospheric
507 stability. *J Clim* 19:6425–6432

508 Wyant MC, Bretherton CS, Blossey PN, Khairoutdinov M (2012) Fast cloud adjustment to increasing CO₂ in a
509 superparameterized climate model. *J Adv Model Earth Syst* 4:M05001. doi:10.1029/2011MS000092

510 Xu KM, Li Z, Cheng A, Hu Y (2018) Changes in clouds and atmospheric circulation associated with rapid
511 adjustment induced by increased atmospheric CO₂: a multiscale modeling framework study. *Clim Dyn*.
512 doi:10.1007/s00382-018-4401-2

513 Zhang C (1993) Large-scale variability of atmospheric deep convection in relation to sea surface temperature in
514 the tropics. *J Clim* 6:1898–1913

515 Zelinka M, Klein S, Taylor K, Andrews T, Webb M, Gregory J, Forster P (2013) Contributions of different cloud
516 types to feedbacks and rapid adjustments in CMIP5. *J Clim* 26:5007–5027

517 Zhou C, Zelinka MD, Klein SA (2016) Impact of decadal cloud variations on the Earth's energy budget. *Nat Geosci*
518 9:871–874

519

520

521 **Table captions**

522

523 **Table 1.** Decomposition of climate response to quadrupling CO₂ using ACCESS1.0. Simulation names in the
524 second column refer Run I.D. in Ackerley et al. (2018). Model configuration, experimental setup, and their
525 results are detailed in Ackerley and Dommenges (2016) and Ackerley et al. (2018)

526

527 **Table 2.** Responses of cloud fraction and EIS to quadrupling CO₂. Values indicate 15-model ensemble means and
528 its 95% confidence intervals. Cal & Can column indicates area-averaged anomaly over low cloud regions off
529 the coasts of California and the Canary Islands (Fig. 1c). SST < 27°C column indicate anomaly over cool
530 ocean (SST < 27°C) between 70°S and 70°N. Winter and summer columns indicated seasonal-mean anomalies
531 determined by May-to-September and November-to-March in the two hemispheres (see Figs. 1 and 2)

532

533 **Table 3.** Similar to Table 2, but for shortwave cloud radiative effect at the top of the atmosphere (SWcld; W m⁻²).
534 Global column indicated global-mean anomaly including land and ocean

535

536 **Table 4.** Decomposed cloud, EIS and SWcld response to quadrupling CO₂ averaged over cool oceans (SST <
537 27°C) using ACCESS1.0

538

539 **Figure captions**

540

541 **Fig. 1** Seasonality in the cloud adjustment to quadrupling CO₂ simulated in 15 CMIP5 models. (a–c) Annual mean
542 anomaly in cloud fraction over ocean (%). (d–f) Wintertime (November-to-March in the Northern
543 Hemisphere and May-to-September in the Southern Hemisphere, respectively) and (g–i) summertime (May-
544 to-September in the Northern Hemisphere and November-to-March in the Southern Hemisphere,
545 respectively) anomalies. (a, d, g) Anomalies in total cloud fraction (ΔC_t), (b, e, h), sum of high cloud (ΔC_h)
546 and middle cloud (ΔC_m), and (c, f, i) low cloud (ΔC_l). Stipples indicate the area where at least 12 out of 15
547 models agree on sign of the anomaly. Contours in (c, f, i) indicate climatological sea surface temperature
548 (SST) of 27 °C. Boxes in (c, f, i) indicate low cloud regions off the coasts of California and the Canary
549 Islands examined in Table 2

550

551 **Fig. 2** Similar to Fig. 1, but for (a, d, g) surface air temperature (ΔSAT ; K), (b, e, h) air temperature at the 700 hPa
552 level (ΔT_{700} ; K), and (c, f, i) estimated inversion strength (ΔEIS ; K), respectively

553

554 **Fig. 3** (a) Zonal-mean ΔEIS (K) over cool oceans (SST < 27 °C). Red and blue lines indicate summertime and
555 wintertime averages, respectively. Shading represents 95% confidential interval. (b) ΔC_l (%) over cool oceans
556 (SST < 27 °C)

557

558 **Fig. 4** Similar to Figs. 2f and 1f, but for summertime minus wintertime anomaly

559

560 **Fig. 5** Annual-mean total response to quadrupling CO₂ simulated in ACCESS1.0. (a) ΔSAT (K), (b) ΔT_{700} (K),
561 (c) ΔEIS (K), (d) ΔC_t (%), (e) $\Delta C_h + \Delta C_m$ (%), and (f) ΔC_l (%). Contours in (f) indicate climatological SST
562 of 27 °C

563

564 **Fig. 6** Decomposed annual-mean low cloud response simulated in ACCESS1.0. (a) Effect of atmospheric radiation
565 (RAD_ATM) on ΔC_l (%). (b) Effects of plant physiological response (PLANT), (c) radiative land
566 warming (RAD_LAND), and (d) residual (RES)

567

568 **Fig. 7** Similar to Fig. 6, but for $\Delta C_h + \Delta C_m$ (%)

569

570 **Fig. 8** Similar to Fig. 7, but for ΔEIS (K)

571

572 **Fig. 9** Wintertime and summertime response to quadrupling CO_2 simulated in ACCESS1.0. (a–f) Effects of
573 RAD_ATM and (g–l) RAD_LAND on (a, d, g, j) ΔT_{700} (K), (b, e, h, k) ΔEIS (K), and (c, f, i, l) ΔC_1 (%).
574 Left (a–c, g–i) and right panels (d–f, j–l) show wintertime and summertime anomalies

575

576 **Fig. 10** Similar to Fig. 3, but for effects of (a, b) RAD_ATM and (c, d) RAD_LAND to (a, c) ΔEIS (K) and (b, d)
577 ΔC_1 (%) simulated in ACCESS1.0

578

579 **Fig. 11** Effect of RAD_ATM to vertical motion and temperature advection. (a) Wintertime and (c) summertime
580 anomaly in pressure velocity (ω ; hPa day⁻¹) at the 700 hPa level ($\Delta\omega_{700}$). Solid and dashed contours represent
581 climatological ω_{700} of 10 hPa day⁻¹ (downward) and -10 hPa day⁻¹ (upward), respectively. (b) Wintertime and
582 (d) summertime vertical temperature advection and adiabatic compression (K day⁻¹) at the 700 hPa level. (e)
583 Zonal-mean vertical temperature advection and adiabatic compression (K day⁻¹) at the 700 hPa level (blue:
584 winter, red: summer) averaged over cool oceans (SST < 27 °C)

585

586 **Fig. 12** Comparison of instantaneous radiative heating due to quadrupling CO_2 among five climate models. (a–e)
587 Wintertime radiative heating (K day⁻¹) at the 700 hPa level and (f–j) summertime minus wintertime radiative
588 heating simulated in (a, f) CanAM4, (b, g) HadGEM2-A, (c, h) IPSL-CM5A-LR, (d, i) MIROC3, and (e, j)
589 MIROC5. (k–o) Zonal-mean radiative heating (K day⁻¹) averaged over cool oceans (SST < 27 °C)

590

591 **Table 1.**

Name	Definition	Explanation
TOTAL	$A_{4x} - A$	Total effect of 4xCO ₂
RAD_ATM	$A_{4xrad_{PL}} - A_{PL}$	Effect of atmospheric radiation
RAD_LAND	$A_{PL4xrad} - A_{PL}$	Effect of radiative land warming
P_PLANT	$A_{4x_{PL}} - A_{4xrad_{PL}}$	Effect of plant physiological response except soil moisture and soil temperature
P_LAND	$A_{PL4x} - A_{PL4xrad}$	Effect of plant physiological response via soil moisture and soil temperature
PLANT	$P_{PLANT} + P_{LAND}$	Total effect of plant physiological response
RES	$TOTAL - (RAD_ATM + RAD_LAND + PLANT)$	Residual

592

593

594 **Table 2.**

	Cal & Can			SST < 27°C		
	Annual	Winter	Summer	Annual	Winter	Summer
ΔC_i (%)	-0.63 ± 0.40	-0.84 ± 0.36	-0.27 ± 0.50	-0.58 ± 0.34	-0.94 ± 0.33	-0.18 ± 0.41
$\Delta C_h + \Delta C_m$ (%)	-1.19 ± 0.25	-0.79 ± 0.23	-1.59 ± 0.32	-0.91 ± 0.21	-0.74 ± 0.21	-1.07 ± 0.24
ΔC_l (%)	0.21 ± 0.26	-0.46 ± 0.31	1.03 ± 0.35	-0.00 ± 0.22	-0.61 ± 0.27	0.71 ± 0.25
ΔEIS (K)	0.41 ± 0.10	0.08 ± 0.08	0.77 ± 0.13	0.28 ± 0.05	0.12 ± 0.05	0.46 ± 0.05

595

596

597 **Table 3.**

	Global			SST < 27°C		
	Annual	Winter	Summer	Annual	Winter	Summer
ΔSW_{cld} ($W\ m^{-2}$)	1.09 ± 0.49	1.07 ± 0.35	1.09 ± 0.66	1.17 ± 0.51	1.25 ± 0.39	1.07 ± 0.70

598

599

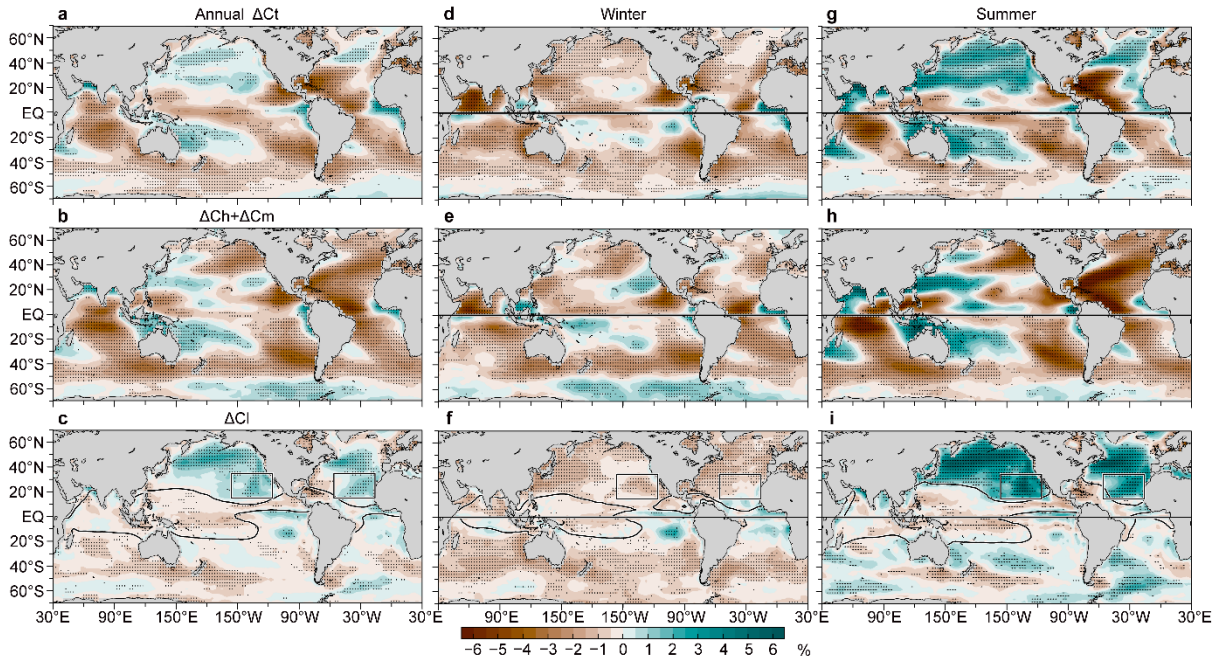
600 **Table 4.**

		Annual	Winter	Summer
ΔC_i (%)	TOTAL	-0.02	-0.53	0.71
	RAD_ATM	-0.11	-0.52	0.37
	RAD_LAND	0.15	-0.01	0.35
	PLANT	-0.13	-0.06	-0.14
	RES	0.07	0.06	0.12
ΔC_i (%)	TOTAL	1.05	0.43	1.89
	RAD_ATM	0.68	0.17	1.26
	RAD_LAND	0.41	0.08	0.75
	PLANT	-0.21	-0.01	-0.38
	RES	0.18	0.19	0.26
ΔEIS (K)	TOTAL	0.32	0.16	0.53
	RAD_ATM	0.25	0.15	0.38
	RAD_LAND	0.11	0.05	0.18
	PLANT	-0.02	0.03	-0.07
	RES	0.01	-0.03	0.07
ΔSW_{cld} ($W\ m^{-2}$)	TOTAL	0.55	0.75	0.17
	RAD_ATM	0.66	0.73	0.49
	RAD_LAND	-0.26	-0.04	-0.57
	PLANT	0.20	0.12	0.30
	RES	-0.05	-0.06	-0.05

601

602

603

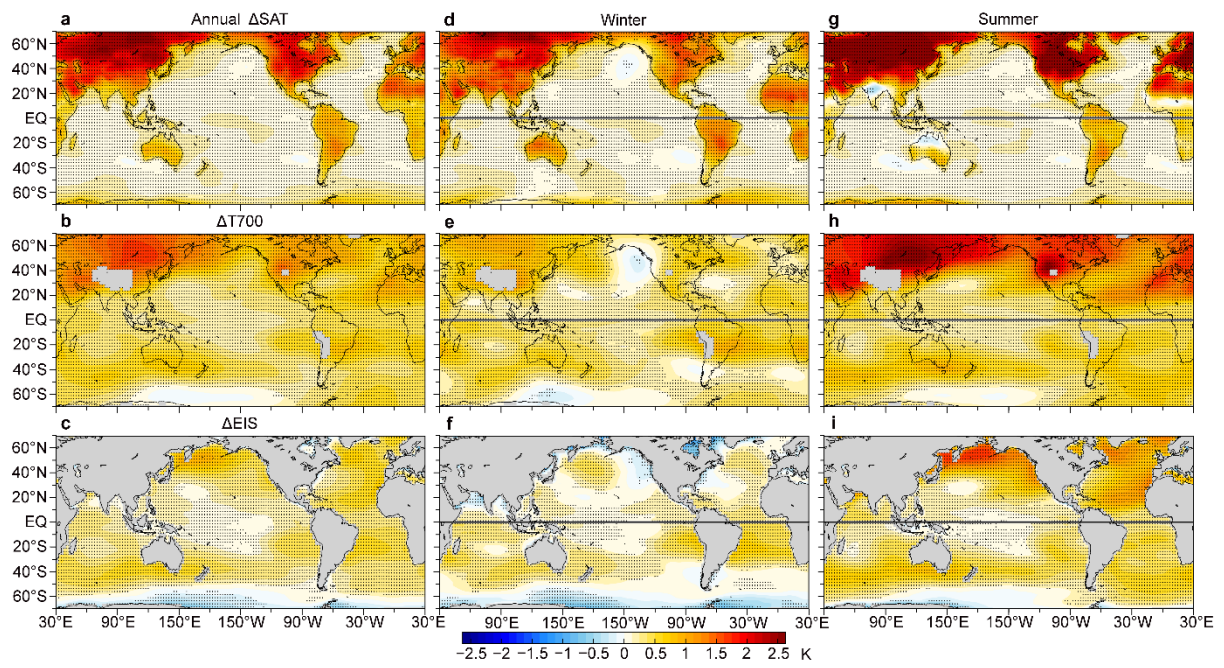


604

605

606 **Fig. 1**

607

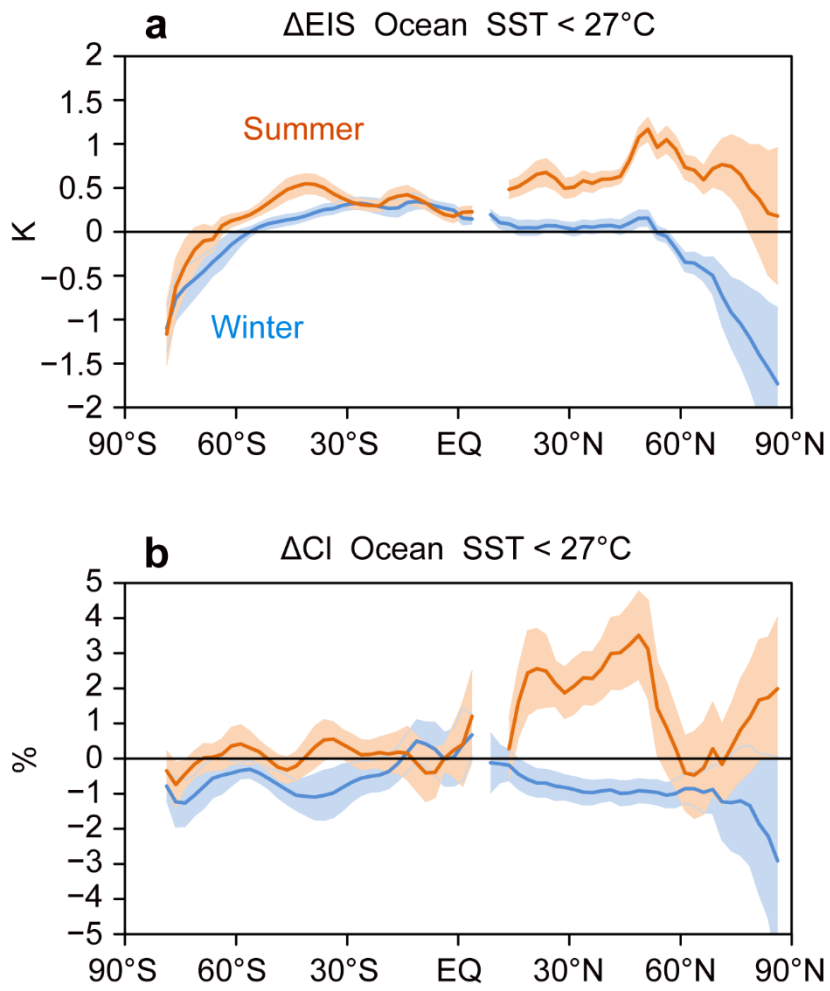


608

609

610 **Fig. 2**

611



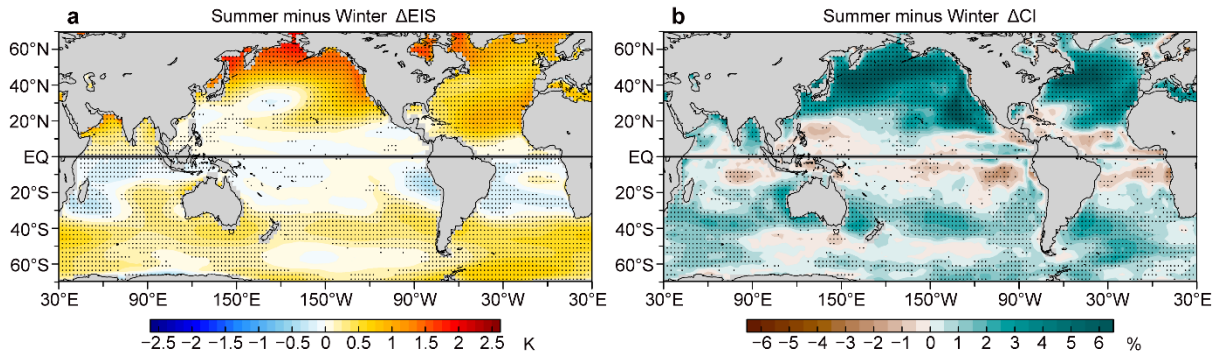
612

613

614 **Fig. 3**

615

616

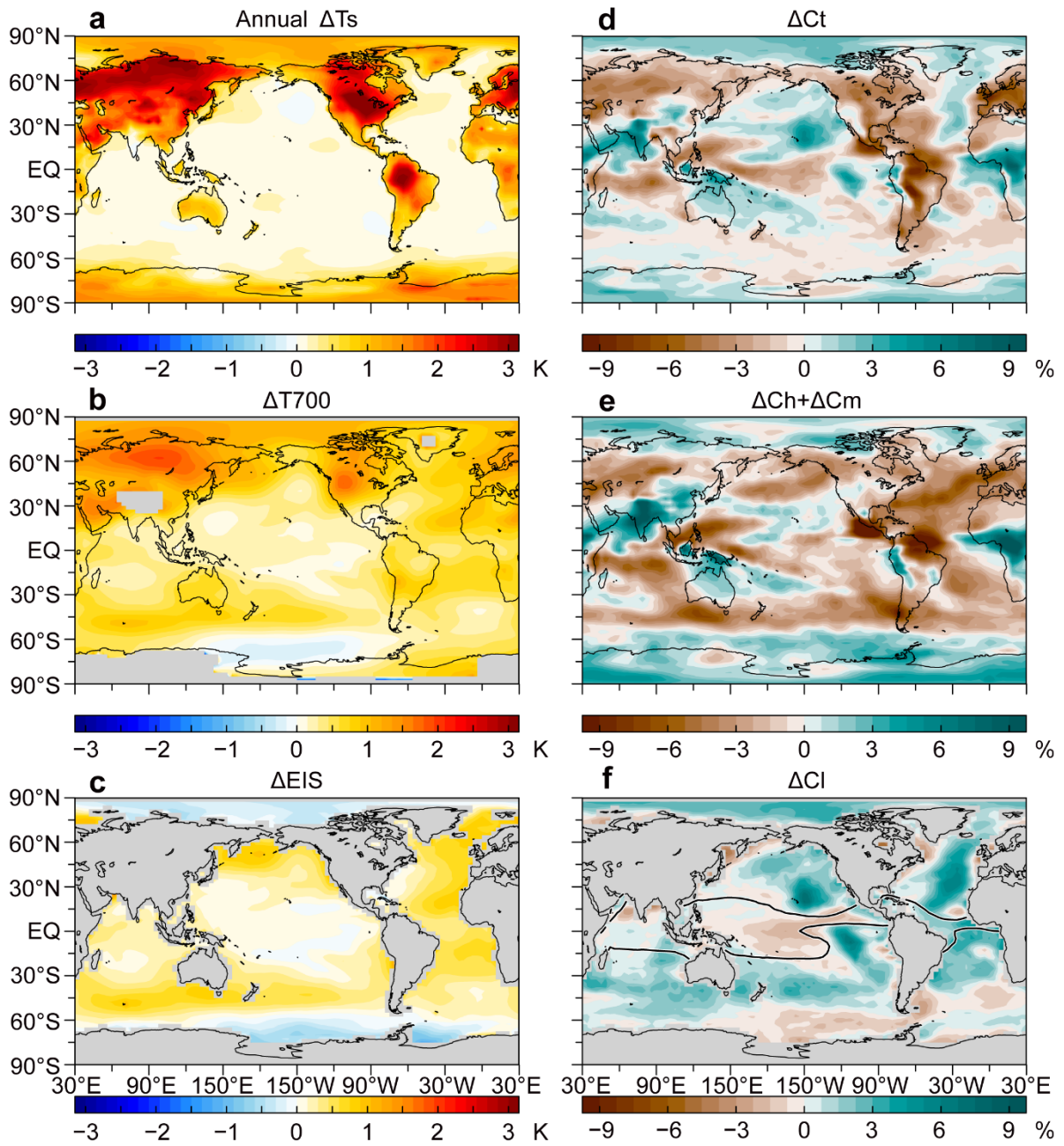


617

618

619 **Fig. 4**

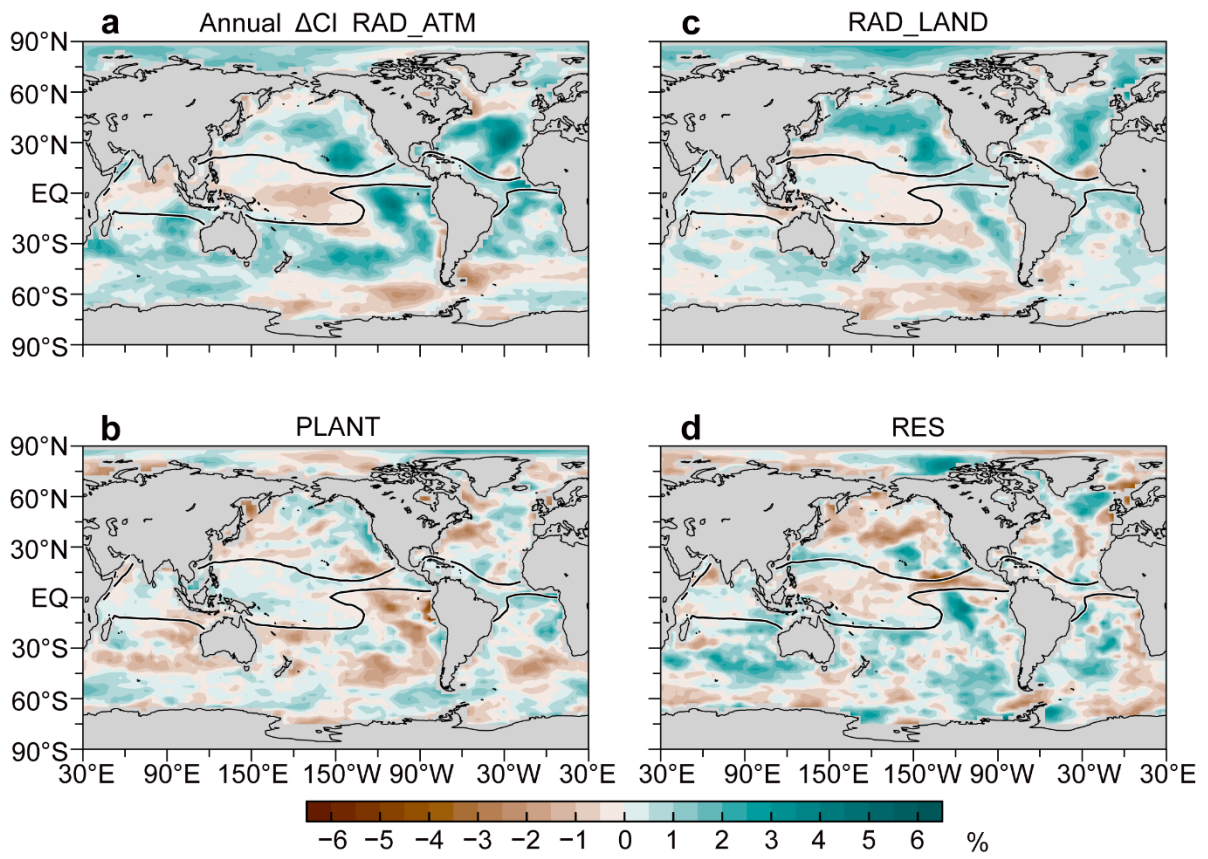
620



621

622

623 Fig. 5

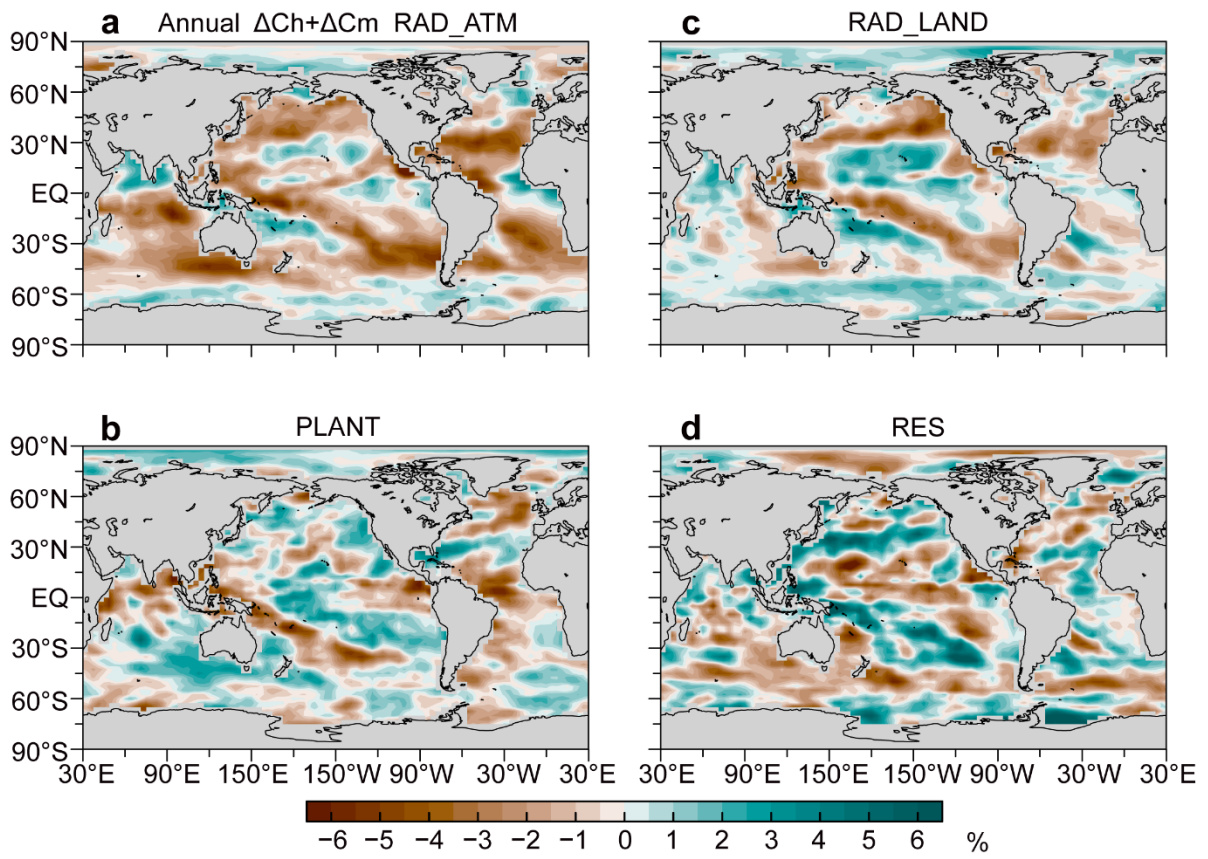


624

625

626 **Fig. 6**

627

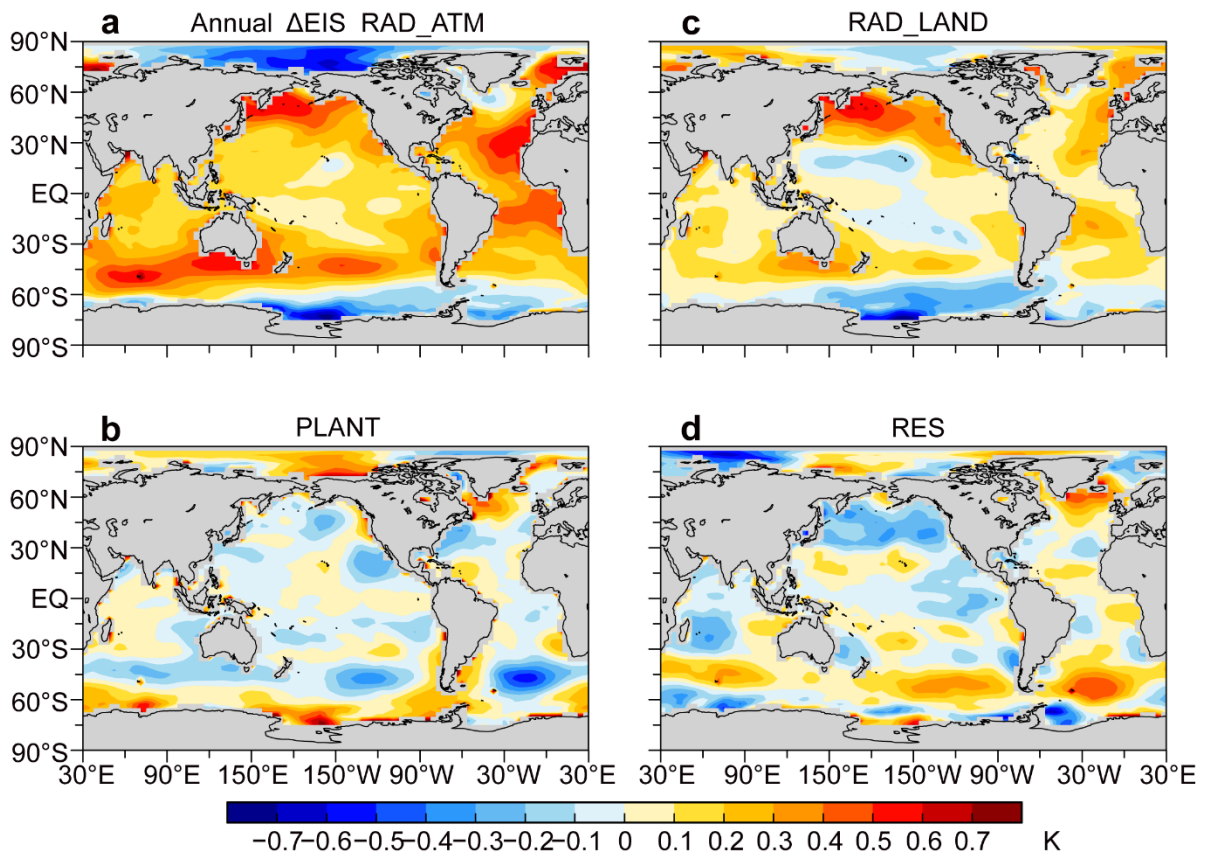


628

629

630 **Fig. 7**

631

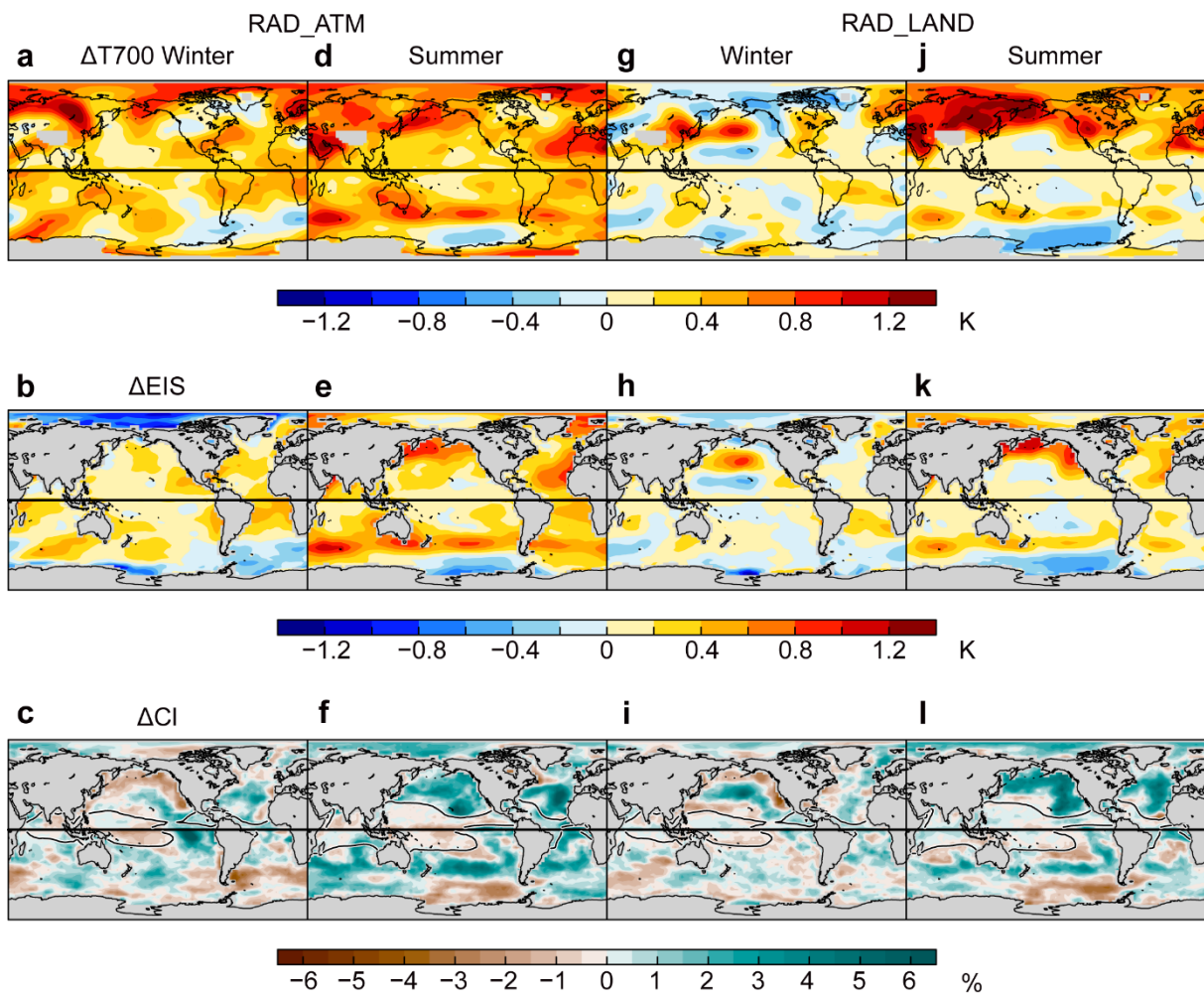


632

633

634 **Fig. 8**

635

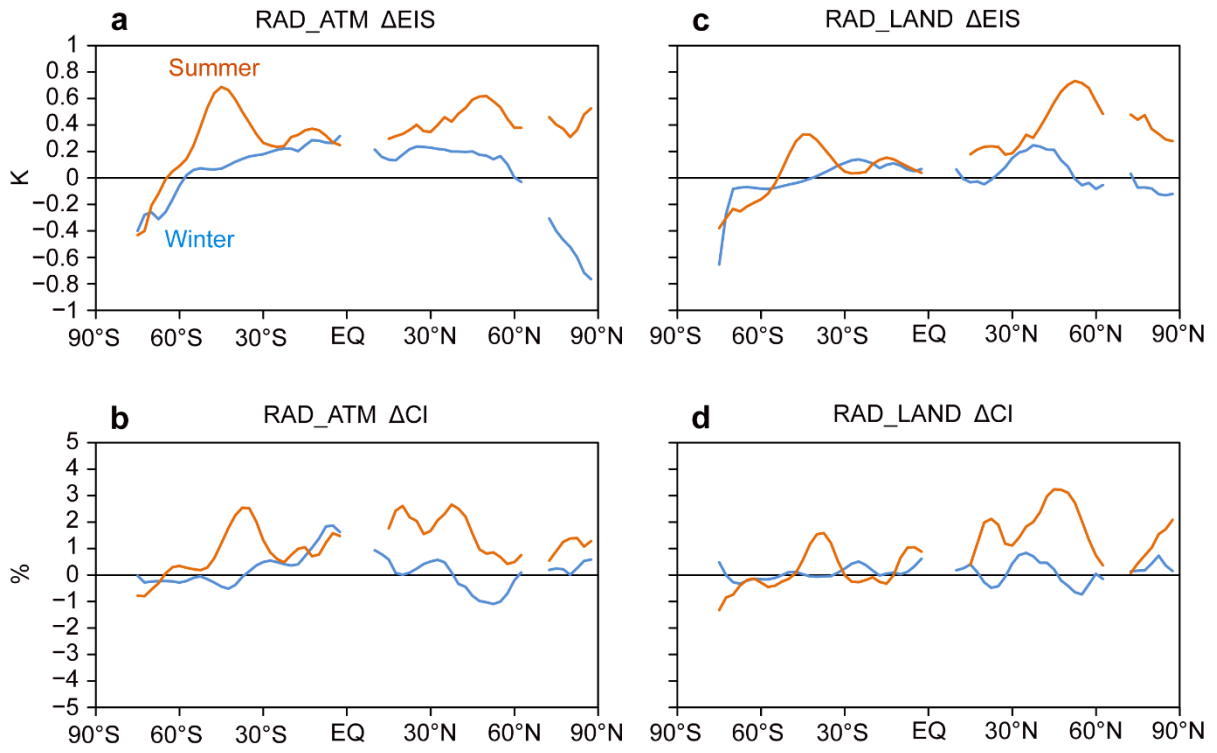


636

637

638 **Fig. 9**

639

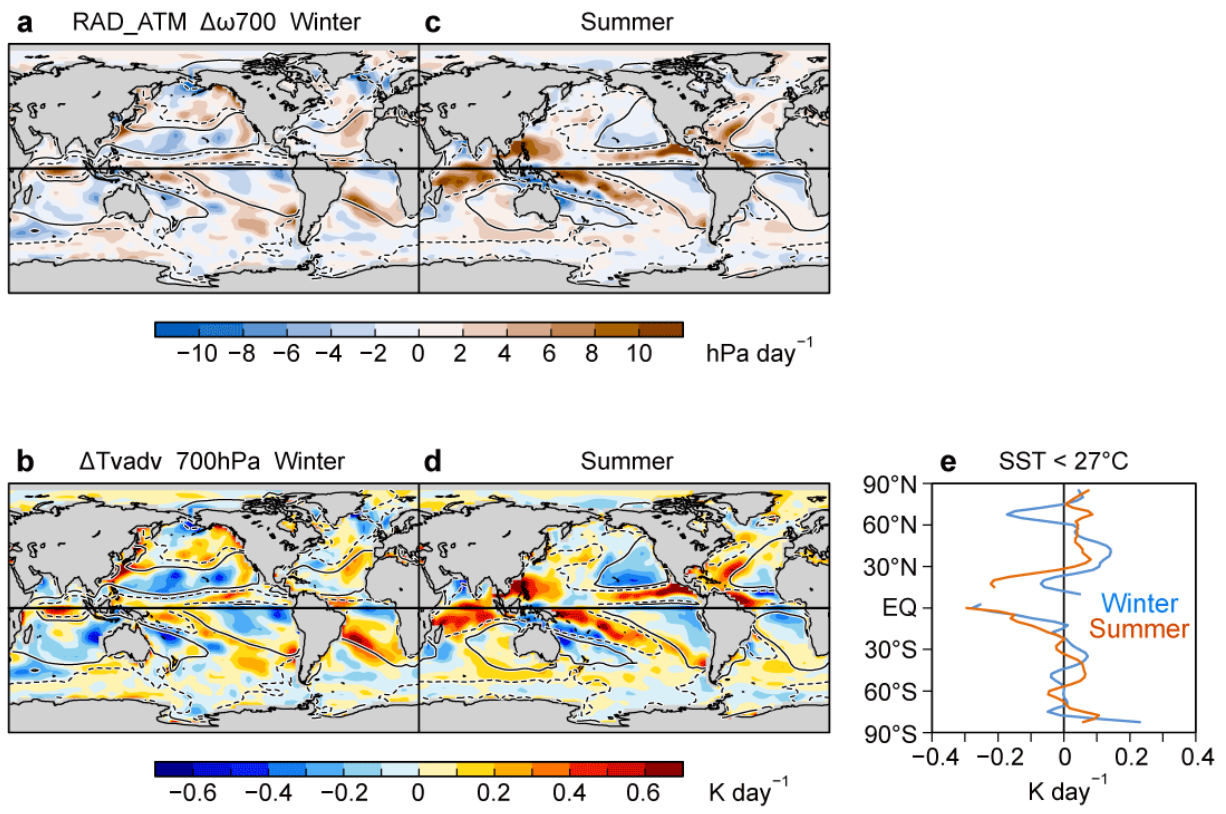


640

641

642 **Fig. 10**

643

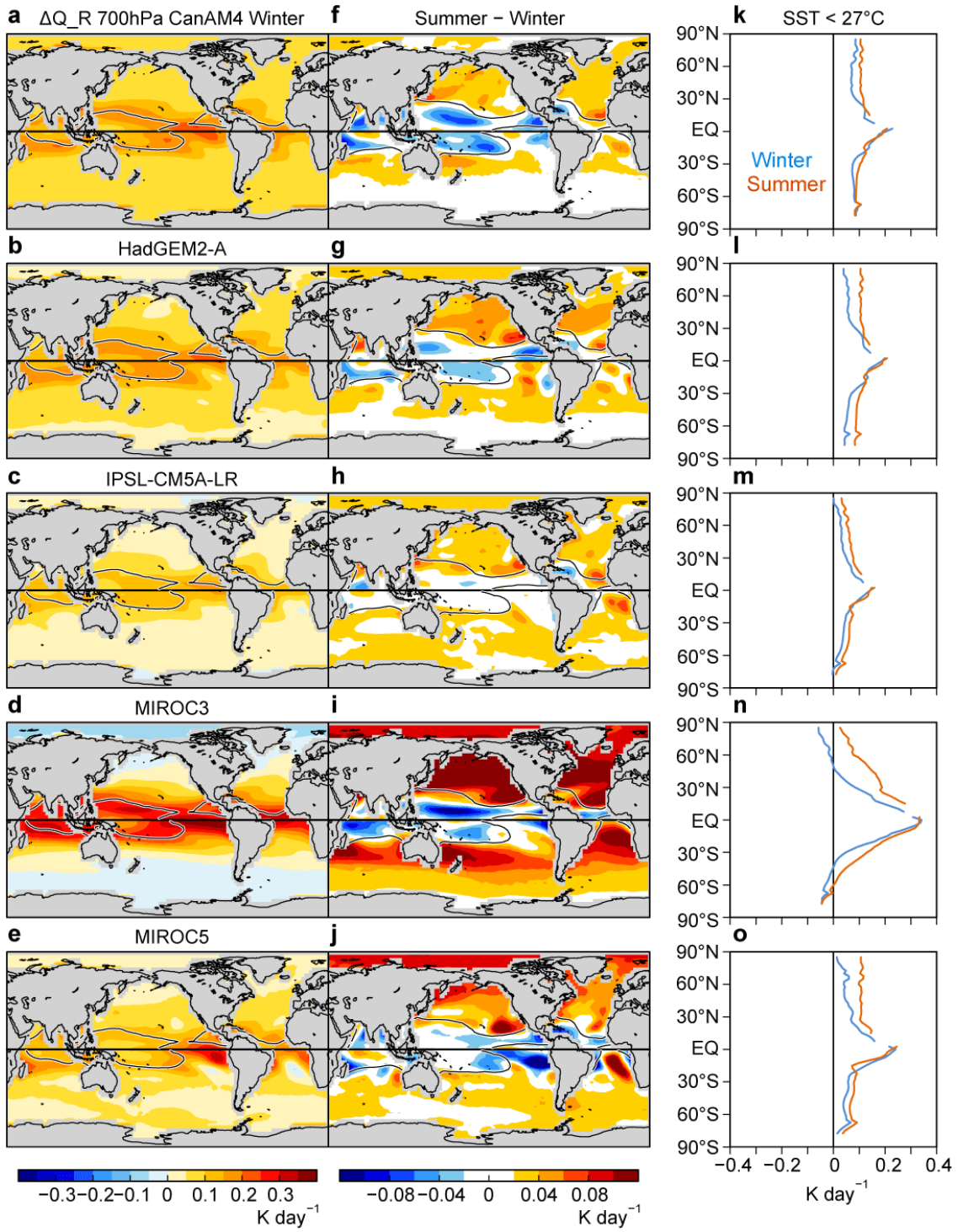


644

645

646 **Fig. 11**

647



648

649

650 **Fig. 12**

651